8

Graphene-Based Devices Based on Topological Zero Modes and Pseudospin Degree of Freedom

J. C. Martinez[1], M. B. A. Jalil[1,3] and S. G. Tan[2,3]
[1]*Information Storage Materials Laboratory, Electrical and Computer Engineering Department, National University of Singapore,*
[2]*Data Storage Institute, A*STAR (Agency for Science, Technology and Research),*
[3]*Computational Nanoelectronics and Nano-device Laboratory, Electrical and Computer Engineering Department, National University of Singapore, Singapore*

1. Introduction

Lately we have witnessed a resurgence of interest in some exotic but hitherto unobserved predictions of relativistic quantum mechanics, particularly in the phenomena of zitterbewegung (Schliemann et al., 2006) and the Klein paradox (Katsnelson et al., 2006). In the former case this interest has been fueled by the realization that bound electrons in suitable semiconductor nanostructures are expected to display zitterbewegung at much lower frequencies and with much larger amplitudes than free electrons. In the latter case, the recently established conducting properties of graphene, an atomic layer of graphite, point to charge carriers moving at speeds close to the Fermi speed ($10^6 \mathrm{m\,s^{-1}}$) which plays the role of light speed for this system (Kane, 2005). In pursuit of these tantalizing developments one might also consider the possibility of harnessing the novel features of graphene for device applications. In this article, we will introduce two concepts which are unique to graphene systems which we believe could be potentially useful for nanodevices.

a. Topological Zero Modes
b. Pseudospin Orbital Coupling

1.1 Topological zero modes

We conjecture that with present day technologies, one might be able to observe the interactions between particle and antiparticle in the low-energy context of bilayer graphene. To introduce the phenomenon we wish to describe let us think for a moment of the game of bowling. One can enjoy it in two ways: a normal person can hurl the ball and be thrilled by strikes and spares, while a child can gently slide the ball on the sidetrack and watch it roll back from the return rack. But another possibility occurs if the ball neither goes for the pins nor comes back but stays put somewhere. Paradoxically this scenario can be more intriguing as one tries to analyze the resting position of the ball. An analogous situation occurs in quantum mechanical tunneling, where electrons are either transmitted or reflected if their kinetic energies are greater or less than the strength of the step-potential barrier they

are incident upon [Landau & Lifshitz, 1968]. However in relativistic quantum mechanics, a third scenario can theoretically arise, namely, spatially-bound particles due to the interaction between particle and antiparticle. Such interplay is unknown in semi-classical or non-relativistic quantum mechanics, and is rarely observed even in relativistic quantum mechanics since the requisite electric fields far exceed available technologies. In this article we will show in Section 3 that this effect can be reproduced in bilayer graphene in the presence of an antisymmetric potential kink.

1.2 Pseusospin orbital coupling

It is well known that electron spin is coupled to its momentum due to the spin orbit coupling effect which can be understood via classical electrodynamics or relativistic quantum mechanics. Dirac's equation predicts that in the presence of electromagnetic fields, a single spin particle experiences the Zeeman and the spin orbit coupling effects. In the latter, one can visualize that an electron traveling with a non-vanishing speed in the electric field, will in its rest frame "see" an effective magnetic field. The magnetic field strength depends on the angle between the momentum and the electric field in the plane which contains both and the field direction is perpendicular to this plane. It is only natural to envisage that the electron spin will precess about this effective magnetic field and that the spin precession would be tightly coupled to electron scattering, due to the dependence of the field strength on the electron motion. What follows is the realization that this phenomenon has useful device properties; indeed, in the last twenty years, numerous transistor designs based upon the Rashba and Dresselhaus spin orbit coupling in semiconductors (Supriyo Datta & B. Das, 1988) have emerged. Bilayer graphene has a Hamiltonian that resembles the massive Dirac system. This led to the idea that an analogy of the above might lead to the design of devices similar to spintronics but in the context of graphene. However, in graphene our focus lies in the pseudospin rather than the real electron spin. A scientific imperative here is to theoretically ascertain the possible existence of such pseudospin orbit coupling and details of this would be presented in Section 4 of this article.

2. Brief introduction to bilayer dynamics

Much has been said about the novelty of graphene which promises new electronics with applications wild and aplenty. The reduced Hamiltonian of bilayer graphene has been the center stage for trapping the "bowling ball" and generating a slew of topological dynamics, as described in Section 1. We will begin with a brief introduction to the full bilayer graphene Hamiltonian leading to its reduced form. As is well known, the bilayer graphene comprises two monolayer graphene stacked vertically and has a more complicated energy structure. The bilayer graphene Hamiltonian (McCann & Fal'ko, 2006) has been expressed as:

$$H_1\psi_1 = \begin{pmatrix} u/2 & v_3\pi & 0 & c\pi^+ \\ v_3\pi^+ & -u/2 & c\pi & 0 \\ 0 & c\pi^+ & -u/2 & t \\ c\pi & 0 & t & u/2 \end{pmatrix} \begin{pmatrix} \varphi_{A1} \\ \varphi_{B2} \\ \varphi_{A2} \\ \varphi_{B1} \end{pmatrix} \tag{1}$$

where $\pi = p_x + ip_y$ and $t = \varepsilon\gamma$. In graphene it is known that interlayer coupling between A_1 and B_2 is strong. Subscripts A, B refer to the sublattice index, while 1, 2 refer to the layer index. Alternatively there are different versions of the Hamiltonian found in the literature. The differences arise mainly from symmetry as well as variations due to approximations.

Bilayer Graphene Hamiltonian

1. $$H_1\psi_1 = \begin{pmatrix} u/2 & v_3\pi & 0 & c\pi^\dagger \\ v_3\pi^\dagger & -u/2 & c\pi & 0 \\ 0 & c\pi^\dagger & -u/2 & t \\ c\pi & 0 & t & u/2 \end{pmatrix} \begin{pmatrix} \varphi_{A1} \\ \varphi_{B2} \\ \varphi_{A2} \\ \varphi_{B1} \end{pmatrix}$$

(McCann, E et al, 2006)

2. $$H_2\psi_2 = \begin{pmatrix} -u/2 & c\pi^\dagger & 0 & 0 \\ c\pi & -u/2 & t & 0 \\ 0 & t & u/2 & c\pi^+ \\ 0 & 0 & c\pi & u/2 \end{pmatrix} \begin{pmatrix} \varphi_{A1} \\ \varphi_{B1} \\ \varphi_{A2} \\ \varphi_{B2} \end{pmatrix}$$

(Martin, Ivar et al 2008); (Manes, J.L. et al, 2007)

3. $$H_3\psi_3 = \begin{pmatrix} -u/2 & c\pi^\dagger & 0 & v_3\pi \\ c\pi & -u/2 & t & 0 \\ 0 & t & u/2 & c\pi^+ \\ v_3\pi^\dagger & 0 & c\pi & u/2 \end{pmatrix} \begin{pmatrix} \varphi_{A1} \\ \varphi_{B1} \\ \varphi_{A2} \\ \varphi_{B2} \end{pmatrix}$$

Table 1. Hamiltonian of the bilayer graphene resembles the massive Dirac Hamiltonian

The spinor wavefunction of (1) in Table I above is different from those in (2) and (3). A transformation can be performed as follows

$$\psi = \begin{pmatrix} \psi_{A1} \\ \psi_{B2} \\ \psi_{A2} \\ \psi_{B1} \end{pmatrix} \rightarrow \psi' = U\psi = \begin{pmatrix} \varphi_{A1} \\ \varphi_{B1} \\ \varphi_{A2} \\ \varphi_{B2} \end{pmatrix}, \quad \text{where } U = \begin{pmatrix} 1 & 0 & 0 & 0 \\ 0 & 0 & 0 & 1 \\ 0 & 0 & 1 & 0 \\ 0 & 1 & 0 & 0 \end{pmatrix} = U^+ \tag{2}$$

It is not hard to see that U defined above has the property of: Hermicity, i.e. $U = U^+$ and Unitarity, i.e. $UU^+ = 1$. The Hamiltonian can then be transformed using $H^t = UHU^+$. In summary we have

$$H_1\psi_1 = \begin{pmatrix} u/2 & v_3\pi & 0 & c\pi^+ \\ v_3\pi^+ & -u/2 & c\pi & 0 \\ 0 & c\pi^+ & -u/2 & t \\ c\pi & 0 & t & u/2 \end{pmatrix} \begin{pmatrix} \phi_{A1} \\ \phi_{B2} \\ \phi_{A2} \\ \phi_{B1} \end{pmatrix} \rightarrow H_1^t\psi_1^t = \begin{pmatrix} u/2 & c\pi^+ & 0 & v_3\pi \\ c\pi & u/2 & t & 0 \\ 0 & t & -u/2 & c\pi^+ \\ v_3\pi & 0 & c\pi & -u/2 \end{pmatrix} \begin{pmatrix} \phi_{A1} \\ \phi_{B1} \\ \phi_{A2} \\ \phi_{B2} \end{pmatrix} \tag{3}$$

The Hamiltonian H_1^t is identical to H_3 and is very close to that of H_2 (see Table 1) except that $v_3\pi$ and $v_3\pi^{+1}$ have been dropped in H_2. It will be interesting to inspect if the above Hamiltonian fit the Dirac's equation exactly, which in its standard form is given by

$$\begin{pmatrix} E-mc & -\boldsymbol{\sigma}\cdot\boldsymbol{p} \\ \boldsymbol{\sigma}\cdot\boldsymbol{p} & -E+mc \end{pmatrix}\psi = 0 \tag{4}$$

To achieve greater transparency, we manipulate the Dirac's equation slightly by simply multiplying both sides of the Hamiltonian α_0 $\frac{i\hbar\partial_0}{c} = \gamma\cdot p + mc$ with γ_0, which then leads to $\frac{i\hbar\partial_0}{c} = \gamma_0\vec{\gamma}\cdot\vec{p} + \gamma_0 mc = \hbar\gamma_5\vec{\boldsymbol{\sigma}}\cdot\vec{\partial} + \gamma_0 mc$. Recalling that $\alpha_0 = \gamma_0 = \begin{pmatrix} I & 0 \\ 0 & -I \end{pmatrix}, \gamma_0\gamma_0 = 1;\ i\gamma_5 = \begin{pmatrix} 0 & 1 \\ 1 & 0 \end{pmatrix}$, one could obtain straightforwardly that $i\gamma_5\boldsymbol{\sigma}\cdot\boldsymbol{p} + \gamma_0 mc = \begin{pmatrix} mc & \boldsymbol{\sigma}\cdot\boldsymbol{p} \\ \boldsymbol{\sigma}\cdot\boldsymbol{p} & -mc \end{pmatrix}$. The energy equation can thus be written as follows

$$\begin{pmatrix} E-mc & -\boldsymbol{\sigma}\cdot\boldsymbol{p} \\ -\boldsymbol{\sigma}\cdot\boldsymbol{p} & E+mc \end{pmatrix}\psi = 0 \tag{5}$$

which seems to be a closer fit with H_1. The above shows that bilayer graphene Hamiltonian mimics that of the massive Dirac systems to some extent. Future nanofabrication technologies, which afford us greater control over the various interlayer and sublattice coupling strengths, might allow us to produce a graphene-like system with closer correspondence to the massive Dirac system.

Reduction of the Bilayer Graphene Hamiltonian

In bilayer graphene, the 4x4 Hamiltonian is cumbersome, and one often uses a 2x2 simplified form. We will in this section simplify the larger bilayer graphene Hamiltonian. We will use H_3 as an example

$$H_3\psi_3 = \begin{pmatrix} -u/2 & c\pi^+ & 0 & v_3\pi \\ c\pi & -u/2 & t & 0 \\ 0 & t & u/2 & c\pi^+ \\ v_3\pi^+ & 0 & c\pi & u/2 \end{pmatrix}\begin{pmatrix} \varphi_{A1} \\ \varphi_{B1} \\ \varphi_{A2} \\ \varphi_{B2} \end{pmatrix} = \begin{pmatrix} -\frac{u}{2}\varphi_{A1} + c\pi^+\varphi_{B1} + v_3\pi\varphi_{B2} \\ c\pi\varphi_{A1} - \frac{u}{2}\varphi_{B1} + t\varphi_{A2} \\ t\varphi_{B1} + \frac{u}{2}\phi_{A2} + c\pi^+\varphi_{B2} \\ v_3\pi^+\varphi_{A1} + c\pi\varphi_{A2} + \frac{u}{2}\varphi_{B2} \end{pmatrix} \tag{6}$$

where u is the applied electrical voltage between the two layers; t is the interlayer coupling. One assumes here that in the limit of strong interlayer coupling, i.e. $t >> u$, occupancy at sites A2 and B1 become zero. It thus follows from Eq. (6) that

$$\begin{pmatrix} -\frac{u}{2}\varphi_{A1} + c\pi^+\varphi_{B1} + v_3\pi\varphi_{B2} \\ c\pi\varphi_{A1} - \frac{u}{2}\varphi_{B1} + t\varphi_{A2} \\ t\varphi_{B1} + \frac{u}{2}\varphi_{A2} + c\pi^+\varphi_{B2} \\ v_3\pi^+\varphi_{A1} + c\pi\varphi_{A2} + \frac{u}{2}\varphi_{B2} \end{pmatrix} = E\begin{pmatrix} \varphi_{A1} \\ \varphi_{B1} \\ \varphi_{A2} \\ \varphi_{B2} \end{pmatrix} = E\begin{pmatrix} \varphi_{A1} \\ 0 \\ 0 \\ \varphi_{B2} \end{pmatrix} \tag{7}$$

resulting in the following set of equations: $c\pi\varphi_{A1} - \frac{u}{2}\varphi_{B1} + t\varphi_{A2} = 0$ and $t\varphi_{B1} + \frac{u}{2}\varphi_{A2} + c\pi^{+}\varphi_{B2} = 0$. Solving these in the limit of $t >> u$, one obtains:

$$\phi_{A2} = -\frac{2c\,\pi\, t\varphi_{A1} + c\pi^{+}u\varphi_{B2}}{2t^2}; \quad \phi_{B1} = \frac{c\,\pi u\varphi_{A1} - 2c\pi^{+}t\varphi_{B2}}{2t^2} \tag{8}$$

and with proper substitution, one obtains:

$$\begin{pmatrix} -\frac{u}{2}(1-\frac{c^2p^2}{t^2})\varphi_{A1} - \frac{c^2\pi^{+2}}{\mathrm{t}}\varphi_{B2} + v_3\pi\varphi_{B2} \\ 0 \\ 0 \\ -\frac{c^2\pi^2}{t}\varphi_{A1} + v_3\pi^{+}\varphi_{A1} + \frac{u}{2}(1-\frac{c^2p^2}{t^2})\varphi_{B2} \end{pmatrix} = E\begin{pmatrix} \varphi_{A1} \\ \varphi_{B1} \\ \varphi_{A2} \\ \varphi_{B2} \end{pmatrix} \tag{9}$$

which leads to the simplified Hamiltonian for $H_3\psi_3$ of

$$H_3^S\psi_3^S = \begin{pmatrix} -\frac{u}{2}(1-\frac{c^2p^2}{t^2}) & 0 & 0 & (-\frac{c^2\pi^{+2}}{t} + v_3\pi) \\ 0 & 0 & 0 & 0 \\ 0 & 0 & 0 & 0 \\ (-\frac{c^2\pi^2}{t} + v_3\pi^{+}) & 0 & 0 & \frac{u}{2}(1-\frac{c^2p^2}{t^2}) \end{pmatrix}\begin{pmatrix} \varphi_{A1} \\ 0 \\ 0 \\ \varphi_{B2} \end{pmatrix} \tag{10}$$

from which one could write in 2x2 form

$$H\begin{pmatrix} \varphi_{A1} \\ \varphi_{B2} \end{pmatrix} = \begin{pmatrix} -\frac{u}{2}(1-\frac{c^2p^2}{t^2}) & (-\frac{c^2\pi^{+2}}{t} + v_3\pi) \\ (-\frac{c^2\pi^2}{t} + v_3\pi^{+}) & \frac{u}{2}(1-\frac{c^2p^2}{t^2}) \end{pmatrix}\begin{pmatrix} \varphi_{A1} \\ \varphi_{B2} \end{pmatrix} \tag{11}$$

The energy equation of the reduced bilayer graphene can now be written as

$$E = -\frac{c^2}{t}\begin{pmatrix} 0 & \pi^{+2} \\ \pi^2 & 0 \end{pmatrix} - \frac{u}{2}(1-\frac{c^2p^2}{t^2})\begin{pmatrix} 1 & 0 \\ 0 & -1 \end{pmatrix} + v_3\begin{pmatrix} 0 & \pi \\ \pi^{+} & 0 \end{pmatrix} \tag{12}$$

The approximation which has been adopted above is related to present-day fabrication technologies. Future advances in technologies might allow us to engineer the various coupling parameters in graphene. It is conceivable that we may be able to pre-design a useful Hamiltonian and employ the nanofabrication technologies to realize that desired form of Hamiltonian. The Hamiltonian above has been used to understand the presence of topological objects like monopoles in graphene and their associated Berry's phase which may have great implications to electron, or perhaps we may just call them (Dirac) particle dynamics or conductance (Novoselov, et al.,2006; Tan, et al, 2010).

3. Topological zero mode device

The phenomenon we briefly described in Section 1 requires a particle-antiparticle pair to be held apart by an external electrostatic field and yet be strongly correlated. For Dirac electrons the typical energy is $O(mc^2)$ and the corresponding correlation length is the Compton wavelength $\hbar/mc$ (Itzykson & Zuber, 1980), implying a restraining electric field of the order of $10^{17}\ \mathrm{V\,m^{-1}}$, a field far beyond present-day capabilities. But we may use bilayer graphene whose top speed is 300 times smaller than c and the excitation mass one-twentieth of the electron's (Castro Neto et al. 2009). (As we will explain below, here chiral pairs replace particle-antiparticle pairs.) Then the electric field needed is 10 orders of magnitude smaller, or $10^{7}\ \mathrm{V\,m^{-1}}$, which is accessible with present technology. Monolayer graphene under these circumstances would generate a different mechanism, more akin to the Zener breakdown, and quite unrelated to our purpose (Martinez et al. 2010).

We therefore study a gated bilayer graphene configuration with an impressed voltage kink V to provide a restraining potential for a particle and its chiral partner. Such kinks can be produced for instance in a graphene p-n junction (Abanin & Levitov, 2007). Recently it has been shown that such configurations can support zero modes and chiral states in the vicinity of the domain wall separating the insulating regions (Martin et al., 2008). If the bias $V(x)$ in the form of a kink is applied between the layers then the motion in the y-direction is that of a free particle and the dynamics in the x-direction will be the one of interest. We will show that a charged particle with energy less than the bias will not undergo total reflection as expected quantum mechanically but will remain in the vicinity of the kink and can manifest itself as charge bound to the kink. The system turns out to be able to support zero modes, occurring *always* at the same value of the particle's y-momentum, and the Hall conductivity plateaus in its vicinity correspond to those of the graphene monolayer. Moreover we find other bound states as well as scattering states as the energy of the particle is raised above the kink strength. All these imply that the kink introduces new and unexpected features into the bilayer dynamics which are externally adjustable. Due to the relativistic and topological nature of our results, we expect them to be of general interest in other non-graphene areas of investigation, e.g., particle physics (Horava, 2005) and superconductivity (Lu & Yip, 2008).

As we saw in Section 2 the low-energy Hamiltonian for the graphene bilayer is a 4×4 matrix in the space spanned by the four-component wave function. It can be reduced further into a reasonably accurate effective 2×2 matrix if we are interested only in the lowest-energy bands, i.e., when the interlayer hopping between nearest neighbors is much larger than the electron energy (measured from zero momentum). If we model the kink potential as an anti-symmetric tanh profile imposed by the electrostatic bias and introduce appropriate scales, the effective 2×2 wave equation is (Martin et al., 2008; cf. Eq. (12))

$$\begin{pmatrix} -(e+r\ \tanh x) & \left(\frac{d}{dx}+p_y\right)^2 \\ \left(\frac{d}{dx}-p_y\right)^2 & -(e-r\ \tanh x) \end{pmatrix} \begin{pmatrix} u(x) \\ v(x) \end{pmatrix} = 0\,, \tag{13}$$

where r $(0\le r\le 1)$ denotes the bias and p_y the particle momentum in the y-direction, e a scaled energy (Fig. 1). In this section only e denotes energy. This effective Hamiltonian involves the atomic sites (A_1, B_2). Thus the 'spinor' structure of Eq. (13) has nothing to do with spin; rather it refers to the electron occupancy at these atomic sites. The qualification

'chiral' is thus applied to this case. We will refer to the equations obtained from Eq. (13) as the first and second component equations, respectively. Formally Eq. (13) can be reduced into a single equation because it is clear that one component converts to the other through the replacement $x \to -x$. Thus, a possible set of solutions to Eq. (13) can be obtained, in which their two components are related by $u(x) = \pm v(-x)$. Equation (13) has been treated as two separate problems, one for $\Psi = (u(x),\ u(-x))^T$ and another for $\Phi = (u(x),\ -u(-x))^T$. However, we will not adopt this approach here, since the resulting solutions would appear to imply a *nonlocal* relation between $u(x)$ and $u(-x)$ for the *entire* range of x: in other words, we would obtain differential equations involving $u(x)$ and $u(-x)$ (and similarly for $v(x)$) simultaneously and for every x. In this system, as defined by Eq. (13), there is no underlying symmetry to support such a relation. In the absence of bias (r = 0), the above system can easily be solved using local relations. In the presence of bias, which is local as well, there is no reason to introduce a nonlocality whereby the dynamics at $+x$ (for given x) is directly related to that at $-x$, and for all x. Thus, we follow an alternative method below, in which *local* relations (i.e. occurring at the *same* spatial point) between $u(x)$ and $v(x)$ will suffice to obtain an exact solution: hence *all* dynamical relations will connect phenomena at the *same* spatial point. This point will be reinforced at several places in this section. Hence, our result differs from those of Martin et al. (2006).

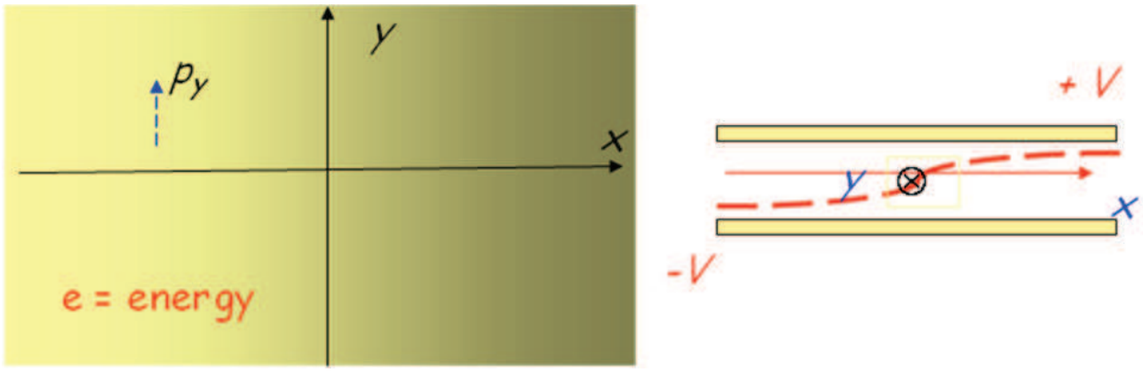

Fig. 1. Views of the bilayer system top (left) and side (right) with kink potential $V(x) = r \tanh x$.

To solve Eq. (13) exactly we introduce the ansatz for $x \geq 0$:

$$\begin{pmatrix} u \\ v \end{pmatrix} = e^{-\xi x} \begin{pmatrix} U(x) \\ V(x) \end{pmatrix}, \tag{14}$$

where ξ is a complex number and we replace x with the auxiliary variable $z = -e^{-2x}$. Our focus is principally, though not exclusively, on the intragap solutions, $|e| \leq r$, and we give explicit expressions for r = 1. We obtain for the first component of Eq. (13):

$$(1-z)\,z\,V'' + (1-z)(1-p_y+\xi)V' - \tfrac{1}{2}U = 0, \tag{15}$$

where ' denotes d/dz. In arriving at Eq. (15) we had imposed the eigenvalue relation $(p_y - \xi)^2 V - (e+1)U = 0$, whose consistency will be verified later. Plugging this

relation for U into Eq. (15) we obtain a hypergeometric equation for $V(x)$ alone with the solution (Abramowitz & Stegun, 1964)

$$V(x) = {}_2F_1(a,\ b,\ c,\ z), \tag{16}$$

$a = \frac{1}{2}(p_y - \xi)(-1 + \sqrt{\frac{e-1}{e+1}}), b = \frac{1}{2}(p_y - \xi)(-1 - \sqrt{\frac{e-1}{e+1}}), c = 1 - p_y + \xi$, and ${}_2F_1(a, b, c, z)$ is the Gauss hypergeometric series and the parameters a, b, c depend only on the energy and p_y. (Useful properties of the hypergeometric equation are listed in the Appendix.) The second equation can be solved similarly:

$$V(x) = \frac{(p_y + \xi)^2}{e-1}\,{}_2F_1(A,\ B,\ C,\ z), \tag{17}$$

$A = \frac{1}{2}(p_y + \xi)(-1 + \sqrt{\frac{e+1}{e-1}}), B = \frac{1}{2}(p_y + \xi)(-1 - \sqrt{\frac{e+1}{e-1}}), C = 1 + p_y + \xi$, with corresponding eigenvalue relation $(p_y + \xi)^2 U - (e-1)V = 0$. (A technical point is in order: when solving the second equation one finds the roles of U and V reversed. This is a veiled signal that locality is crucial because any assumed nonlocal relation, except possibly for overall sign, invoked for the first equation would not generally be consistent for the second.) Together the two relations yield a consistency condition implying an independent equation relating ξ, e and p_y: writing $\xi = a + i\beta$, we solve this equation to obtain $a(\beta) = \frac{1}{\sqrt{2}}[(p_y^4 + 1 - e^2)^{1/2} + (-)p_y^2]^{1/2}$. This ensures the consistency of the ansatz (14) and the eigenvalue relations: any dependence on x, U, or V has now been eliminated in favor of an algebraic one involving e and p_y alone. Implicit in the above development is the locality of all the intervening relations, that is, all dynamical relations between u and v occur at the *same* spatial point x. The complex conjugates of (16) and (17) are easily seen to be solutions of Eq. (15) also so we can form a linear combination of these to arrive at the complete ($x \geq 0$) solution. Next the above procedure can be repeated for $x < 0$. Replacing ξ with $-\xi$ in the ansatz (14) and employing a new auxiliary variable, $y = -e^{2x}$, we discover that the solutions are exactly the same ones (15) and (17) above but with the order reversed and z replaced by y. The numbers a and β are given by the same relation above. (Thus there are four solutions of which, for $x \geq 0$ ($x \leq 0$), we choose a positive (negative). There is no such restriction on β). We summarize these results: corresponding to Eq. (16)

$$V(x) = {}_2F_1(a',\ b',\ c',\ y), \quad x < 0 \tag{16a}$$

$a' = \frac{1}{2}(p_y + \xi)(1 + \sqrt{\frac{e+1}{e-1}}), b' = \frac{1}{2}(p_y + \xi)(1 - \sqrt{\frac{e+1}{e-1}}), c' = 1 + p_y + \xi$, and to Eq. (17),

$$V(x) = \frac{(p_y - \xi)^2}{e+1}\ {}_2F_1(A',\ B',C',y), \quad x<0\ , \tag{17a}$$

$A' = \frac{1}{2}(p_y - \xi)(-1+\sqrt{\frac{e-1}{e+1}})$, $B' = \frac{1}{2}(p_y - \xi)(-1-\sqrt{\frac{e-1}{e+1}})$, $C' = 1 - p_y + \xi$. Once again the eigenvalue relations enforce a local connection between $V(x)$ and $U(x)$. With these, we have evaluated the complete intragap solutions for $e < 1$.

A glance at Eq. (17) suggests that it may not be valid for $e = 1$. However, on writing the eigenvalue relation in the form $p_y + \xi = \sqrt{e^2 - 1}/(p_y - \xi)$, we note that as $e \to 1^-$, both sides approach zero. Employing this result to carry out a limiting procedure on Eq. (17), we obtain the $e = 1$ solution: $\frac{1}{2p_y^2} e^{p_y x}\ {}_2F_1\ (1/2p_y, -1/2p_y\ ,\ 1,\ z)$. For this solution to remain bound for $x \geq 0$ we must have $p_y < 0$, which can be verified later once the dispersion graphs have been obtained (see Fig. 1).

There remains the problem of enforcing continuity between the $x \geq 0$ and $x \leq 0$ solutions. Restricting to the first equation, we form the linear combination $g_>(x)$ $= e^{-ax}\ {}_2F_1\ (a,b,c,z)\ (c_1 e^{i\beta x} + c_2 e^{-i\beta x})$, for $x \geq 0$ and c_1 and c_2 complex constants; a similar expression, $g_<(x)$, holds for $x \leq 0$ with the signs of x reversed, a replaced by $-a$, and with coefficients c_3 and c_4 instead. As intragap solutions, these functions are normalizable, and the coefficients c_i are determined by demanding that $g_>(x)$, $g_<(x)$ and their first three derivatives be continuous at $x = 0$. These yield four homogeneous simultaneous equations and we use the requirement that the determinant of the system must vanish to derive the dispersion relation, $e = e(p_y)$. Clearly, the only independent dynamical parameter is the energy, e. The same procedure is repeated for the second equation (parameters a, b, c are exchanged with A, B, C and vice versa), in which case we use the label $h(x)$ instead of $g(x)$, and we obtain a pair of complete solutions for the two components of Eq. (13), respectively which we write in schematic form (for $x \geq 0$)

$$\begin{pmatrix} u(x) \\ v(x) \end{pmatrix} = g_>(x) \begin{pmatrix} (p-\xi)^2/(e+1) \\ 1 \end{pmatrix}, h_>(x) \begin{pmatrix} 1 \\ (p+\xi)^2/(e-1) \end{pmatrix}. \tag{18}$$

The procedure outlined above produced *two* pairs (18) but there is really only *one* pair of solutions. Examining these solutions, we notice that one set can be obtained from the other by the formal substitution $p_y \to -p_y$ and $e \to -e$ and multiplying the spinors by $-i\sigma_y$. (We had also made use of the symmetry of the hypergeometric solutions given in the Appendix.) Hence the solutions (18) are really chiral conjugates of the each other. This can be shown formally by transforming Eq. (13) into its chiral conjugate form, wherein the sign of the energy *and* p_y are reversed. First we write Eq. (13) as

$$\begin{pmatrix} -\varphi(x) & \pi^{+2} \\ \pi^{-2} & \varphi(x) \end{pmatrix} \begin{pmatrix} u(x) \\ v(x) \end{pmatrix} = e \begin{pmatrix} u(x) \\ v(x) \end{pmatrix} \tag{19}$$

where $\varphi(x)$ denotes the kink potential and $\pi^{\pm} = d/dx \pm p_y$. Now we multiply both sides by σ_y and cast the result in the form

$$\begin{pmatrix} -\varphi(x) & \pi^{-2} \\ \pi^{+2} & \varphi(x) \end{pmatrix} \sigma_y \begin{pmatrix} u(x) \\ v(x) \end{pmatrix} = (-e) \begin{pmatrix} u(x) \\ v(x) \end{pmatrix} \tag{20}$$

This tells that $(u,v)^T$ is conjugate to $\sigma_y\ (u,v)^T$, in the sense that one is obtained from the other by the substitution $p_y \to -p_y$ and $e \to -e$, consistent with the results above. By virtue of the electron-hole symmetry of the graphene Hamiltonian, this results in the chiral symmetry between the solutions.

Recall that the original graphene Hamiltonian was derived within the tight-binding model (Gonzalez et al., 1993). One can view our system in terms of a set of coupled oscillators, so the states $(1, 1)^T$ and $-i\sigma_y (1, 1)^T = (-1, 1)^T$ represent the two distinct and independent normal modes, one being symmetric, the other antisymmetric. These symmetries are global and affect the entire system. The procedure outlined above to solve Eq. (13) assumes no global symmetry. The conclusion from this comparison is not a relation between $u(x)$ and $u(-x)$ (implying nonlocality) but the chiral nature of these solutions (which is local). This harks back at the local 'spinor' structure of Eq. (13).

3.1 Discussion

We have plotted the dispersion relations $e = e(p_y)$ in Fig. 2. Notice the $e \to -e,\ p_y \to -p_y$ symmetry of the curves. In Fig. 2 (a) the two initial ($r = 0$) parabolic bands of the bilayer have the form $e = \pm p_y^2$ and these are separated as the biasing potential grows (Fig. 2 (b) and (c)) thus creating a gap between the bands. The parabolic bands then take the form $e = \pm\sqrt{p_y^4 + r^2}$. As we will see below these separated bands correspond to over-barrier scattering states which do not decay on account of the potential. For the intragap states, two zero modes appear symmetrically about the origin. A more detailed examination of the zero modes in Fig. 2(b) and (c) suggests that they occur at the same p_y value for *any* non-zero bias $(r \neq 0)$. This is indeed correct and can be shown explicitly by making use of the method presented in Section 3. We can give for instance the zero-mode wave functions V obtained from the first equation for any value of r

$$\begin{aligned} V_{>}^{e=0}(x) &= c_1\ e^{-\xi x}\ {}_2F_1\left(\frac{p_y-\xi}{\sqrt{2}} e^{3i\pi/4},\ \frac{p_y-\xi}{\sqrt{2}} e^{-3i\pi/4},\ 1-p_y+\xi,\ z\right) + cc \\ V_{<}^{e=0}(x) &= c_3\ e^{-\xi x}\ {}_2F_1\left(\frac{p_y+\xi}{\sqrt{2}} e^{i\pi/2},\ \frac{p_y+\xi}{\sqrt{2}} e^{-i\pi/2},\ 1+p_y+\xi,\ 1/z\right) + cc \end{aligned} \tag{21}$$

where $p_y = \pm 0.1255$, cc denotes the complex conjugate of the function to the left of it and ξ is defined in Section 2. Although there is no r dependence in Eq. (21), we find that the expressions for U, namely, $U_{>(<)}(x) = \pm\frac{1}{r}(p_y \mp \xi)^2 V_{>(<)}(x)$, contain an r-dependence.

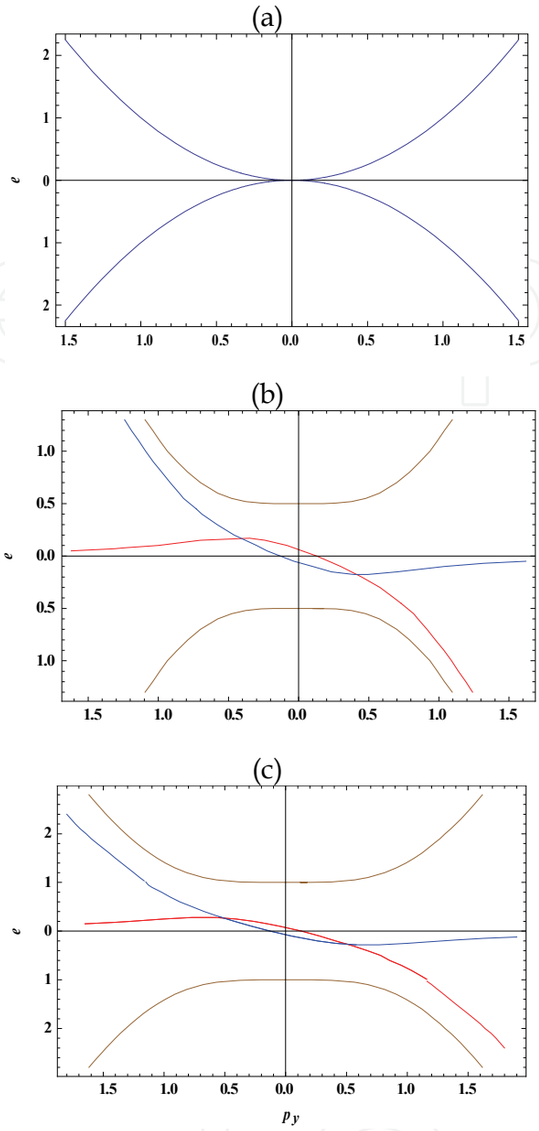

Fig. 2. Dispersion relations for (a) $r = 0$, (b) $r = ½$ and (c) $r = 1$. Zero modes occur at $e = 0$, $p_y = \pm 0.1255$. Note that the $e = 1$ solution has $p_y < 0$. The brown curves correspond to over-barrier scattering states.

The zero modes of our system are not Dirac fermions but chiral modes specific to the bilayer. The fact that these modes occur provided a bias of any strength is present is an indication of the topological character of the kink. That a kink is dynamically necessary is clear because the decay of the wave functions as $x \to \pm\infty$ requires the chiral pair to be close to each other near the origin. Each particle of the pair in turn is held in place by this electrostatic bias (with opposite signs on both sides of $x = 0$) along with the interaction with its conjugate. We can check the consistency of the above from a computation of the topological charge of the Fermi point. Writing the Hamiltonian (13) (without e) as $\vec{\varphi}(\vec{p}, x) \cdot \vec{\sigma}$, this topological charge is given by (Volovik, 2003)

$$N_3 = \frac{1}{8\pi}\varepsilon^{abc}\varepsilon_{ijk}\int_\Sigma dS^k \hat{\varphi}^a \partial_{p_i}\hat{\varphi}^b \partial_{p_j}\hat{\varphi}^c \tag{22}$$

where Σ is a surface enclosing the origin of the p-plane and may be taken to be two infinite planes parallel to the $p_x - p_y$ plane, one to the right and the other to the left of the origin (the separation between the planes being infinitesimal). See Fig. 3. This charge gives the difference between the number of right-moving and left-moving zero modes. Then, $N_3 = 2$, since we must sum the contributions from the right side and left sides of Σ. This is clearly consistent with our results. The existence of the zero modes can be exploited in some applications, as we will point out below.

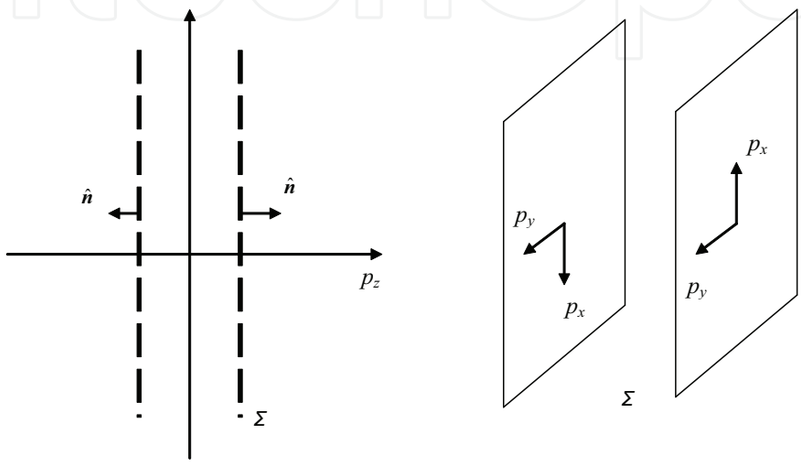

Fig. 3. Two views of the surface Σ with outward normals $\hat{\boldsymbol{n}}$ shown. Note that the p_z-separation between planes is non-zero provided $r \neq 0$. The contribution to the integrand (22) vanishes as $p_x, p_y \to \pm\infty$.

We can show that the Hamiltonian (13) reduces to the monolayer case in the vicinity of the zero mode, i.e., $|e| << 1$. Take for definiteness $U = V$ and assume $U = f\,g$, f being the zero-mode solution. g is a slowly varying function of e which has the value of 1 at $e = 0$, and varies over a length scale which is much larger than the kink width. If we substitute U into the Eq. (13) we obtain $(ip_x + p_y)^2 fg = g(ip_x + p_y)^2 f + 2(ip_x + p_y)f(ip_x + p_y)g + f(ip_x + p_y)^2 g$. The first term, when combined with the kink potential $-V f g$, vanishes for the zero mode f. The second contains the factor $(ip_x + p_y)f = (p_y - (a \pm i\beta))f + e^{-(\alpha \pm i\beta)x}\frac{d}{dx}{}_2F_1(a,b,c,e^{-2x})$. We can neglect the derivative because it will yield an additional factor e^{-2x} (which is small over the length scale of g), while the eigenvalue condition allows us to replace $p_y - (a \pm i\beta))$ with unity for a zero mode. Thus the Hamiltonian for g is $\begin{pmatrix} 0 & ip_x + p_y \\ -ip_x + p_y & 0 \end{pmatrix}$ correct to $O(e^2)$, which is of the form $\vec{\sigma}\cdot\vec{p}_\perp$, where $\vec{p}_\perp$ is perpendicular to the zero-mode momentum. Thus, at the vicinity of the zero mode (around e = 0), the Hamiltonian mimics that of monolayer graphene, with its energy spectrum having the characteristic $\sqrt{N}$ signature (Li & Andrei, 2007; Gusynin & Sharapov, 2005).

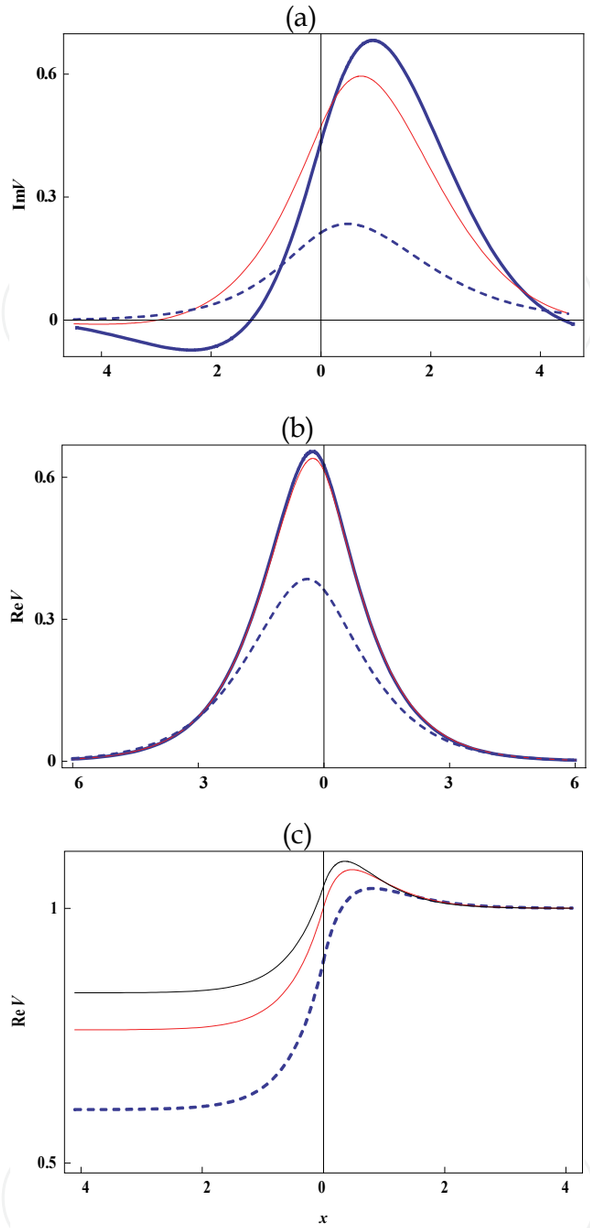

Fig. 4. Wave functions. (a) Imaginary part of the intragap wave function (unnormalized) for $r = 1$: thick blue (e = 0, $p_y = 0.1255$, i.e. the zero mode); dashed, blue ($e = -0.8$, $p_y = 1.03$); red ($e = 0.28$, $p_y = -0.58$). The real parts are much smaller (about a tenth) than the imaginary parts. (b) Real part of wave functions for the $r = 1$, $e > 1$, bound case: dashed blue ($e = 1.1$, $p_y = -1.2$); red ($e = 2.1$, $p_y = -1.69$); thick blue ($e = 2.2$, $p_y = 1.73$). (c) Over-barrier scattering wave functions (unnormalized): black ($e = 2.5$, $p_y = 1.514$); red ($e = 2$, $p_y = 1.316$), blue, dashed ($e = 1.5$, $p_y = 1.057$). The imaginary parts are very small.

Graphs of the dominant (real or imaginary) part of the wave functions are shown in Fig. 4. These figures imply that both the real and imaginary parts of the wave function are important. (By contrast, Martin *et al*. (2008) only find real wave functions.) As displayed in

Fig. 4, the intragrap states appear to always penetrate into the potential so their maxima are found inside it. Although all the intragap states are always bound, they are not the only bound states. In general, whenever the kinematic inequality $p^4 \neq e^2 - 1$ holds, we have bound states because in this case what we really have is $p^4 > e^2 - 1$: this is always the case for the intragap states, but it is also true of the blue and red $|e| > 1$ spiral arms in Figs. 2(b) and (c), a consequence of the fact that not enough of the total energy has been allotted to the motion in the *x*-direction. For these bound $|e| > 1$ states we see in Fig. 4 that their maxima lie to the left of the origin: these states do not penetrate into the kink as deeply as the intragap states do.

When $|e| > 1$ *and* $p^4 = e^2 - 1$, the particles have sufficient energy to overcome the barrier and we have the overbarrier scattering case (the particles go $x \to \pm\infty$). The same procedure for intragap states can be applied, with the factor $e^{-\xi x}$ in Eq. (14) excluded since we are looking for undamped solutions. Some wave functions of this type are given in Fig. 4(c). One can calculate the transmission and reflection amplitudes for them. These suggest greater transmission than reflection.

Because any negative energy eigenstate is related to a positive energy eigenstate by a unitary transformation, the local density of states $\rho(r) = \sum_e \psi_e^+(r)\,\psi_{e'}(r)\,\delta(e - e')$ is symmetric about $e = 0$ and the negative and positive energy eigenstates contribute equally. Including the zero modes, the conservation of the total number of states implies that the difference in densities with and without the kink $\delta\rho$ is

$$0 = \int d^2 r \left(2\int_{-\infty}^{0^-} \delta\rho(r,e)de + |\psi_0(r)|^2 \right) \tag{23}$$

The two zero modes are normalized, so the integral of $\delta\rho$ over energy and space is – 1. Taking electron spin into account this means a charge of – 2*e* and total spin zero for the valence band. If the zero modes are unoccupied, the charge and spin for the kink are, respectively, Q = -2*e* and S = 0; if the zero modes are singly (doubly) occupied, then Q = -*e* (0), S = ½ (0). These serve as the signature of the presence of charge and the confinement of the chiral pair in the vicinity of the kink. Since the zero modes occur in pairs we do not see charge fractionalization here (Hou et al., 2007). Moreover, we need not be concerned here with a violation of Kramer's theorem (Su et al., 1980).

4. Pseudospin orbit coupling (pseudo-SOC) device

By the Dirac equation, spin orbit coupling can be derived in the vacuum with applied electric fields; one thus visualizes that similar effects should arise for the pseudospin of graphene particles governed by the Dirac equations. Thus pseudo-spin orbit coupling (Tan et al, 2010) can be derived by applying external electric field to a system governed by the graphene Hamiltonian. We will start with H_3 which is not a comparable form to standard Dirac Hamiltoninan. But by transformation e. g. using a unitary matrix U, one can obtain a more compatible form (McCann, E et al, 2006) of H_1

$$H_3\psi_3 = \begin{pmatrix} 0 & c\pi^+ & 0 & v_3\pi \\ c\pi & 0 & t & 0 \\ 0 & t & 0 & c\pi^+ \\ v_3\pi^+ & 0 & c\pi & 0 \end{pmatrix} \begin{pmatrix} \varphi_{A1} \\ \varphi_{B1} \\ \varphi_{A2} \\ \varphi_{B2} \end{pmatrix} \rightarrow H_1\psi_1 = \begin{pmatrix} 0 & v_3\pi & 0 & c\pi^+ \\ v_3\pi^+ & 0 & c\pi & 0 \\ 0 & c\pi^+ & 0 & t \\ c\pi & 0 & t & 0 \end{pmatrix} \begin{pmatrix} \varphi_{A1} \\ \varphi_{B2} \\ \varphi_{A2} \\ \varphi_{B1} \end{pmatrix} \quad (24)$$

The transformation which has been performed by U determines the type of pseudo-spin to be investigated, e.g. by the above method which results in $\chi = (A_1\ B_2)^T$ pseudo-spin is defined by the linear superposition of wavefunction amplitude between site A_1 and B_2. In application to particles which mimic Dirac fermions due to material bandstructure, it would be instructive to replace the coupling mass term of mc^2 for particles in vacuum with a coupling term Δ which arises due to material bandstructure but plays the same role as the mass term, as far as the Dirac matrix is concerned. The coupling term Δ gives rise to the energy dispersion where the effective mass of particles in the materials can be derived; in other words, particle effective mass is a function of Δ but not vice versa. For monolayer graphene, Δ vanishes and it can be derived from the energy dispersion relation that particles behave like massless Dirac fermions. In graphene-like materials, χ can be described as a pseudo-spin which consists of a linear combination of waves due to different sub-lattice sites. The above is, however, merely one example of graphene-like materials which can also be written as

$$\begin{pmatrix} E - \Delta_a & -\boldsymbol{\sigma}\cdot\boldsymbol{p}c \\ -\boldsymbol{\sigma}\cdot\boldsymbol{p}c & E - \Delta_b \end{pmatrix} \cdot \begin{pmatrix} \chi \\ \theta \end{pmatrix} = 0 \quad (25)$$

where in this specific case, $\Delta_a = \begin{pmatrix} 0 & v_3\pi \\ v_3\pi^+ & 0 \end{pmatrix}$ and $\Delta_b = \begin{pmatrix} 0 & t \\ t & 0 \end{pmatrix}$ Multiplying by γ^0 to the left, one obtains the graphene Hamiltonian comparable in form to the general Dirac equation

$$\begin{pmatrix} (E - eV) - \Delta_a & -\boldsymbol{\sigma}\cdot\boldsymbol{p}c \\ \boldsymbol{\sigma}\cdot\boldsymbol{p}c & -(E - eV) + \Delta_b \end{pmatrix} \cdot \begin{pmatrix} \chi \\ \theta \end{pmatrix} = 0 \quad (26)$$

where V is the external potential.
The above can be written in terms of Dirac matrices as follows

$$\gamma^\mu D_\mu - R = 0 \quad (27)$$

where $\gamma^0 = \begin{pmatrix} 1 & 0 \\ 0 & -1 \end{pmatrix}$, $\gamma^j = \begin{pmatrix} 0 & \sigma^j \\ -\sigma^j & 0 \end{pmatrix}$, $R = \begin{pmatrix} \Delta_a & 0 \\ 0 & -\Delta_b \end{pmatrix}$, and $D_\mu = \partial_\mu - \frac{ie}{\hbar}A_\mu$. Multiplying the above to the left with $\gamma^\mu D_\mu + R$ yields

$$\begin{pmatrix} (E - eV)^2 - p^2c^2 - \Delta_a^2 & -ie\hbar c\boldsymbol{\sigma}\cdot\boldsymbol{\mathcal{E}} \\ -ie\hbar c\boldsymbol{\sigma}\cdot\boldsymbol{\mathcal{E}} & (E - eV)^2 - p^2c^2 - \Delta_b^2 \end{pmatrix} \cdot \begin{pmatrix} \chi \\ \theta \end{pmatrix} = 0 \quad (28)$$

where $\mathcal{E}^j/c = -\partial_0 A_j$ is the electric field. We provide the above to merely illustrate the close connection between the bilayer graphene and the vacuum Dirac Hamiltonian, such that useful analogies of pseudo-spin orbit coupling to the vacuum spin orbit coupling can be drawn. Thus, to simplify matter, we temporarily disregard the fact that $\Delta_a = \begin{pmatrix} 0 & v_3\pi \\ v_3\pi^+ & 0 \end{pmatrix}$ and $\Delta_b = \begin{pmatrix} 0 & t \\ t & 0 \end{pmatrix}$. Rather we replace $\Delta_a^2 = \begin{pmatrix} (v_3 p)^2 & 0 \\ 0 & (v_3 p)^2 \end{pmatrix}$ with $\Delta_a^2 = \begin{pmatrix} mc^2 & 0 \\ 0 & mc^2 \end{pmatrix}$ so that one can write $\Delta_a^2 = \Delta I$ where $\Delta = mc^2$. We make an even more drastic assumption that one can write $\Delta_b = \begin{pmatrix} mc^2 & 0 \\ 0 & mc^2 \end{pmatrix} = \Delta I$. With this, Eq.(26) can be reduced to

$$\theta = \frac{\boldsymbol{\sigma}\cdot\boldsymbol{p}c}{E - eV - [\Delta_b]}\chi \tag{29}$$

where $[\Delta_b] = \sqrt{[\Delta_a^2]} = \Delta$. The relativistic energy equation which could be used to describe the analogous effect of pseudo spin orbit coupling, i.e. the coupling of pseudo spin to particle momentum in the presence of electric fields, for Dirac fermions in graphene-like material systems is thus

$$\left[(E - eV)^2 - \Delta_a^2 - p^2c^2 - \frac{ie\hbar c^2}{E - eV - [\Delta_b]}\boldsymbol{\mathcal{E}}\cdot\boldsymbol{p} - \frac{e\hbar c^2}{E - eV - [\Delta_b]}\boldsymbol{\sigma}\cdot(\boldsymbol{\mathcal{E}}\times\boldsymbol{p})\right]\chi = 0 \tag{30}$$

To avoid excessive details into the material science and band structure of graphene, we will take the liberty of assuming that the relation $\Delta_a^2 = \Delta^2 I; \Delta_b = \Delta I$ is satisfied in bilayer graphene or, at least, can be realized by material engineering.

We will now investigate the effects of pseudo SO coupling on the pseudo spin χ. As is well-known, a particle in a SO coupling system experiences an effective magnetic field $\boldsymbol{B}_E = \boldsymbol{p}\times\boldsymbol{\mathcal{E}}$ which couples directly to its momentum vector, thus preserving time-reversal symmetry. In the technology-relevant field of spintronics, such $\boldsymbol{B}_E$ can be used to control the precession of spin when coupled with appropriate momentum constraints (e.g. single mode one-dimensional ballistic transport), similar to gate bias-controlled spin precession via Rashba or Dresselhaus SO coupling in the so-called Datta-Das spin transistor (Supriyo, Datta et al, 1989). On the other hand, spin relaxation is related to electron precession about $\boldsymbol{B}_E$ (D'yakonov, M.I. et al, 1971), which suggests that pseudospin relaxation can be analyzed in analogy to spin relaxation under spin orbit coupling, but in the relativistic limit. In typical graphene-like materials, $\Delta = \sqrt{[\Delta_a^2]} = [\Delta_b]$ is small (10-300 meV for massive fermion, 0 meV for massless fermion). Since kinetic energy $KE << \Delta$ (5 order of magnitude smaller) for the non-relativistic approximation to apply, the corresponding number of non-

relativistic particles is very small. For particles confined to energy range 1-2 order of magnitude smaller than Δ, we consider these particles as relativistic; this prompts the need to analyze the pseudo SO effect in the relativistic limit. One could visualize the pseudo spin precessing about an effective magnetic field which could only be "seen" by the pseudo spin, at a precessional frequency which could be deduced from $\hbar\omega = \sqrt{\hbar ep|\boldsymbol{\mathcal{E}}|c^2/(E-[\Delta_b])}$. With the average velocity given by $\langle\chi|v_\mu|\chi\rangle = \frac{c^2 p}{\sqrt{p^2c^2+[\Delta_a^2]}}$, the precession angle over the Bloch sphere of the pseudospin, for a unit of particle travel length in the relativistic regime is given by:

$$\frac{\Omega}{l} = \frac{\omega}{\langle\chi|v_\mu|\chi\rangle} = \sqrt{\frac{e|\boldsymbol{\mathcal{E}}|(p^2c^2+[\Delta_a^2])}{\hbar(E-[\Delta_b])pc^2}} \tag{31}$$

A series of pseudospin relaxation has been predicted and analyzed for different energy regimes. In summary, it has been studied that Dirac particles in the energy range of $pc \approx 1$ meV (which although is relatively small compared to the energy gap of $\Delta \approx$ 200 – 300 meV, it is large enough to be within the relativistic regime), Eq. (31) reduces to $\frac{\Omega}{l} = \frac{\Delta}{p}\sqrt{\frac{e|\boldsymbol{\mathcal{E}}|}{\hbar c^3}}$. Increasing particle's momentum reduces the precessional angle for a fixed travel length. By contrast, in the ultra-relativistic limit (i.e. massless Dirac particle), Eq.(31) reduces to $\Omega/l = \sqrt{e|\boldsymbol{\mathcal{E}}|/\hbar c}$, which predicts that massless Dirac particle has a constant Ω/l. This can be understood as typically, massless particle travels at the effective speed of light in the medium. In this limit, pseudo spin relaxation becomes independent of particle momentum. In the non-relativistic limit, where $\left(\frac{p^2}{2m} + eV + \frac{\hbar ec^2}{4\Delta^2}\boldsymbol{\sigma}\cdot(\boldsymbol{\mathcal{E}}\times\boldsymbol{p})\right)\boldsymbol{\chi} = \boldsymbol{\varepsilon\chi}$, it is found that $\langle\chi|H_{SC}^{nr}|\chi\rangle = \frac{e\hbar c^2}{4\Delta^2}|\boldsymbol{\mathcal{E}}|p$. The average particle velocity can be approximated as $\langle\chi|v_\mu|\chi\rangle = p/m$, and in a similar manner, the precession angle Ω per unit travelling distance is given by $\Omega/l = e|\boldsymbol{\mathcal{E}}|/4\Delta$, which is independent of particle momentum. Therefore in both non-relativistic and ultra-relativistic limits, Ω/l is independent of the particle momentum. But in the former, Ω/l depends inversely on Δ; such a dependence obviously cannot exist in the ultra-relativistic limit where the coupling mass term vanishes.

Based on the above understanding, we briefly propose that a nanoscale device which consists of a graphene ring and a charged nano-sized dot at the centre would be a suitable platform to utilize the pseudospin orbit coupling of the graphene Dirac particles. The pseudospin orbit strength can be calculated in the relativistic and low energy limits in analogy to spin orbit coupling in semiconductors. Pseudospin orbit coupling strength can be enhanced by accelerating the Dirac particles around the ring, due to the small energy gap in graphene and the large radial electric field due to the charged quantum dot.

5. Conclusions

The zero modes (21) may find possible application in two ways: (a) one can take advantage of the relation (18) applied to the zero modes as a switching indicator and (b) in so far as zero modes are of two types associated with the chiral functions $(1, 1)^T$ and $(-1, 1)^T$, they might store information much as binary bits do. The topological properties of the charge and spin of these zero modes confer a certain degree of robustness to these binary states. Even the presence of some disorder would not alter this conclusion provided the kink retains its topological character. An indication of this is that the zero modes appear even for small *r* value. Further application of the zero modes can be derived from utilizing the valley degree of freedom (or "valleytronics" (Rycerz et al., 2007), which can be modified along the kink direction. Our results would also be of interest in brane theory (Horava, 2005) and superconductivity (Lu & Yip, 2008). We also describe another relativistic effect in graphene, namely, pseudospin orbit coupling (pseudo-SOC) effect. Potentially the pseudo-SOC effect can be used for pseudospin field effect transistor (FET) in much the same way that the physical spin orbit coupling is used for semiconductor spin-FET. The pseudospin orbit coupling strength has to be further enhanced for it to be comparable to the conventional semiconductor-based Rashba effect. Future work which focuses on modifying the graphene structure can potentially enhance this useful pseudo-SOC effect within experimentally accessible parameters.

The support of NRF/NUS under Grants Nos. R-143-000-357-281 and R-263-000-482-112 are gratefully acknowledged.

Appendix

The hypergeometric differential equation is (in general z is complex)

$$z(1-z)\frac{d^2w}{dz^2}+[c-(a+b+1)z]\frac{dw}{dz}-ab\,w=0\,,$$

whose solution is the Gauss series

$${}_2F_1(a,b,c;z)={}_2F_1(b,a,c;z)=\frac{\Gamma(c)}{\Gamma(a)\Gamma(b)}\sum_{n=0}^{\infty}\frac{\Gamma(a+n)\Gamma\Gamma+n)}{\Gamma(c+n)}\frac{z^n}{n!}$$

with circle of convergence on the unit circle $|z|=1$. The series is not defined when c = 0 or a negative integer. We also have applied the useful differential relation

$$\frac{d}{dz}\,{}_2F_1(a,b,c,z)=\frac{ab}{c}\,{}_2F_1(a+1,b+1,c+1,z)$$

When $c - a - b$ is an integer (as in overbarrier scattering), extra care is required to solve the hypergeometric equation. In this case the following is true: two linearly independent solutions of

$$z(1-z)\frac{d^2w}{dz^2}+(1-z)(1-p)\frac{dw}{dz}-\frac{1}{2}q\,w=0\,,$$

are the pair

$$ {}_2F_1(-\tfrac{1}{2}(p+\sqrt{p^2-2q}),\ -\tfrac{1}{2}(p-\sqrt{p^2-2q}),\ 1-p,\ z), $$

$$ (-z)^p\ {}_2F_1(\tfrac{1}{2}(p-\sqrt{p^2-2q}),\ \tfrac{1}{2}(p+\sqrt{p^2-2q}),\ 1+p,\ z). $$

6. References

Abanin, D. A. & Levitov, L. S. (2007) Quantized transport in graphene p-n junctions in a magnetic field *Science*, 317, 5838 (August, 2007) 641 – 643, ISSN 0036-8075

Abramowitz, M. & Stegun, I. (1964) *Handbook of Mathematical Functions,* Dover, New York.

Castro Neto, A. H., Guinea, F., Peres, N. M. R., Novoselov, K. S. & Geim, A. K. (2009) The electronic properties of graphene *Rev. Mod. Phys*. 81, 1 (January, 2009) 109-162, ISSN 0034-6861

D'yakonov M.I., Perel V.I., 1971, *Zh. Eksp. Teor. Fiz.* 60, 1954 (Sov. Phys. JETP 38, 1053 (1971) ISSN 0038-5648).

Gonzalez, J., Guinea, F. & Vozmediano, M. A. H. (1993) The electronic spectrum of fullerenes from the Dirac equation, *Nucl. Phys*. B 406, 3 (October, 1993) 771 – 794, ISSN 0550-3213

Gusynin, V. P. & Sharapov, S. G. (2005) Unconventional integer quantum Hall effect in graphene, *Phys. Rev. Lett*. (for McCann Edward) 95, 14 (September, 2005) 146801, ISSN 0031-9007

Horava, P. (2005) Stability of Fermi surfaces and K theory, *Phys. Rev. Lett*. (for McCann Edward) 95, 1 (July, 2005) 016495, ISSN 0031-9007

Hou, C.-Y. , Chamon, C. & Mudry, C. (2007) Electron fractionalization in two-dimensional graphenelike structures, *Phys. Rev. Lett*. (for McCann Edward) 98, 18 (May, 2007) 186809, ISSN 0031-9007

Itzykson, C. & Zuber, J.-B. (1980) *Quantum Field Theory*, Dover, 10: 0486445682 New York.

Kane, C. L. (2005) Erasing electron mass, *Nature* 438, 7065 (November, 2005) 168 – 170 ISSN 0028-0836

Katsnelson, M. I., Novoselov, K. S. & Geim, A. K. (2006) Chiral tunneling and the Klein paradox in graphene, *Nature Phys*. (for Noveselov) 2, 9 (September, 2006) 620 – 625, ISSN 1745-2473

Landau, L. D. & Lifshitz, E. M. (1968). *Quantum Mechanics,* Elsevier-Science, 0 7506 3539 8, London.

Li, G. & Andrei, E. (2007) Observation of Landau levels of Dirac fermions in graphite, *Nature Phys*. 3, 9 (September 2007) 623 – 627, ISSN 1745-2473

Lu, C.-K. & Yip, S. (2008) Zero-energy vortex bound state in noncentrosymmetric superconductors, *Phys. Rev*. (for Manes) B78, 13 (October, 2008) 132502, ISSN 1098-0121

Manes J.L. et al., (2007) Existence and topological stability of Fermi points in multi-layer graphene, *Phys. Rev.* (for Manes) B 75 (April, 2007) 155424, ISSN 1098-0121

Martin, I, Blanter, Ya. M. & Morpurgo, A. F. (2008) Topological confinement in bilayer graphene *Phys. Rev. Lett*. (for McCann Edward) 100, 3 (January, 2008) 036804, ISSN 0031-9007

Martinez, J. C., Jalil, M. B. A. & Tan, S. G. (2010) Klein tunneling and zitterbewegung and the formation of a polarized *p-n* junction, *Appl. Phys. Lett*. 97, 6 (August, 2010) 062111, ISSN 0003-6951

McCann Edward, Fal'ko Vladimir I., Landau-level degeneracy and quantum Hall effect in a graphite bilayer, Phys. Rev. Lett. 96 (March 2005), 086805, ISSN 0031-9007.

Novoselov, K. S., McCann, E., Morozov, S. V., Fal'ko, V. I., Katsnelson, M. I., Zeitler, U., Jiang, D., Schedin, F. & Geim, A. K. (2006) Unconventional quantum Hall effect and Berry's phase of 2π in bilayer graphene, *Nature Phys.* (for Noveselov) 2, 3 (March, 2006) 177- 180, ISSN 1745-2473.

Rycerz, A., Tworzydlo, J. & Beenaker, C. W. J. (2007) Valley filter and valley valve in graphene, *Nature Phys*. (for Noveselov) 3, 3 (March, 2007) 172 – 175, ISSN 1745-2473

Schliemann, J., Loss, D. & Westervelt, R. M. (2006) Zitterbewegung of electrons and holes in III-V semiconductors quantum wells, *Phys. Rev*. (for Manes) B 73, 8 (February, 2006) 085323, ISSN 1098-0121

Su, W. P., Schrieffer, J. R. & Heeger, A. J. (1980) Soliton excitations in polyacetylene, *Phys. Rev*. B 22, 4 (August, 1980), 2099 – 2111, ISSN 1098-0121.

Supriyo Datta & B. Das, Electronic analog of the electro-optic modulator (1989), Appl. Phys. Lett. 56 (December, 1989) 665 – 667, ISSN 0003-6951.

Tan S. G. et al. (2010) Pseudospin-orbital coupling for pseudospntronic device in graphene, *Magnetism and Mag. Materials* (August, 2010) 322, 2390 – 2394, ISSN 0304-8853.

Tan. S. G., Jalil, M. B. A., & Fujita, T. (2010) Monopole and topological electron dynamics in adiabatic spintronic and graphene systems, *Ann. Phys.* (N.Y.) 325, 8 (August, 2010) 1537-1549, ISSN 0003-4916

Volovik, G. E. (2003). *The Universe in a Helium Droplet,* Oxford, ISBN 13: 978-0-19-956484-2, Clarendon

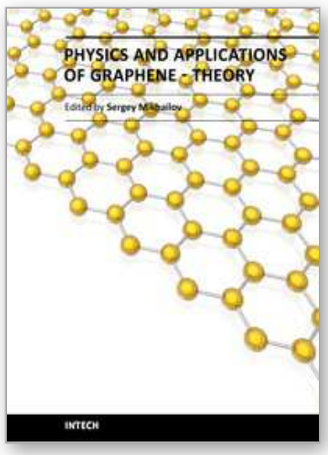

Physics and Applications of Graphene - Theory

Edited by Dr. Sergey Mikhailov

ISBN 978-953-307-152-7
Hard cover, 534 pages
Publisher InTech
Published online 22, March, 2011
Published in print edition March, 2011

The Stone Age, the Bronze Age, the Iron Age... Every global epoch in the history of the mankind is characterized by materials used in it. In 2004 a new era in material science was opened: the era of graphene or, more generally, of two-dimensional materials. Graphene is the strongest and the most stretchable known material, it has the record thermal conductivity and the very high mobility of charge carriers. It demonstrates many interesting fundamental physical effects and promises a lot of applications, among which are conductive ink, terahertz transistors, ultrafast photodetectors and bendable touch screens. In 2010 Andre Geim and Konstantin Novoselov were awarded the Nobel Prize in Physics "for groundbreaking experiments regarding the two-dimensional material graphene". The two volumes Physics and Applications of Graphene - Experiments and Physics and Applications of Graphene - Theory contain a collection of research articles reporting on different aspects of experimental and theoretical studies of this new material.

How to reference

In order to correctly reference this scholarly work, feel free to copy and paste the following:

J. C. Martinez, M. B. A. Jalil and S. G. Tan (2011). Graphene-Based Devices Based on Topological Zero Modes and Pseudospin Degree of Freedom, Physics and Applications of Graphene - Theory, Dr. Sergey Mikhailov (Ed.), ISBN: 978-953-307-152-7, InTech, Available from: http://www.intechopen.com/books/physics-and-applications-of-graphene-theory/graphene-based-devices-based-on-topological-zero-modes-and-pseudospin-degree-of-freedom

INTECH
open science | open minds

InTech Europe
University Campus STeP Ri
Slavka Krautzeka 83/A
51000 Rijeka, Croatia
Phone: +385 (51) 770 447
Fax: +385 (51) 686 166
www.intechopen.com

InTech China
Unit 405, Office Block, Hotel Equatorial Shanghai
No.65, Yan An Road (West), Shanghai, 200040, China
中国上海市延安西路65号上海国际贵都大饭店办公楼405单元
Phone: +86-21-62489820
Fax: +86-21-62489821

IntechOpen